Title

Controlled and Stable Patterning of Diverse Inorganic Nanocrystals on Crystalline Two-Dimensional Protein Arrays

Journal

Biochemistry, 60(13)

ISSN

0006-2960

Authors

Mann, Victor R

Manea, Francesca

Borys, Nicholas J

et al.

Publication Date

2021-04-06

DOI

10.1021/acs.biochem.1c00032

Peer reviewed

HHS Public Access

Author manuscript

Biochemistry. Author manuscript; available in PMC 2021 May 28.

Published in final edited form as:

Biochemistry. 2021 April 06; 60(13): 1063–1074. doi:10.1021/acs.biochem.1c00032.

Controlled and Stable Patterning of Diverse Inorganic Nanocrystals on Crystalline Two-Dimensional Protein Arrays

Victor R. Mann[#1], **Francesca Manea**[#1,2], **Nicholas J. Borys**[1,3], **Caroline M. Ajo-Franklin**[1,4,5,6,*], **Bruce E. Cohen**[1,4,*]

[1]The Molecular Foundry, Lawrence Berkeley National Laboratory, Berkeley, CA 94720

[4]Division of Molecular Biophysics & Integrated Bioimaging, Lawrence Berkeley National Laboratory, Berkeley, CA 94720

[5]Synthetic Biology Institute, Lawrence Berkeley National Laboratory, Berkeley, CA 94720

[6]Department of BioSciences, Rice University, Houston, TX 77005

[2]Current address: Perfect Day Foods, Berkeley, CA 94608

[3]Current address: Department of Physics, Montana State University, Bozeman, MT 59717

[#] These authors contributed equally to this work.

Abstract

Controlled patterning of nanoparticles on bioassemblies enables synthesis of complex materials for applications in optics, nanoelectronics, and sensing. Biomolecular self-assembly offers molecular control for engineering patterned nanomaterials, but current approaches have been limited in their ability to combine high nanoparticle coverage with generality that enables incorporation of multiple nanoparticle types. Here, we synthesize photonic materials on crystalline two-dimensional protein sheets using orthogonal bioconjugation reactions, organizing quantum dots (QDs), gold nanoparticles (AuNPs), and upconverting nanoparticles (UCNPs) along the surface-layer (S-layer) protein SbsB from the extremophile *Geobacillus stearothermophilus*. We use electron and optical microscopy to show that isopeptide bond-forming SpyCatcher and SnoopCatcher systems enable the simultaneous and controlled conjugation of multiple types of nanoparticles (NPs) at high densities along the SbsB sheets. These NP conjugation reactions are orthogonal to each other and to Au-thiol bond formation, allowing tailorable nanoparticle combinations at sufficient labeling efficiencies (up to 30%) to permit optical interactions between nanoparticles. Fluorescence lifetime imaging of SbsB sheets conjugated to QDs and AuNPs at distinct attachment sites shows spatially heterogeneous QD emission, with shorter radiative decays and brighter fluorescence arising from plasmonic enhancement at close interparticle distances.

[*]Contact information: Bruce E. Cohen, The Molecular Foundry and Division of Molecular Biophysics & Integrated Bioimaging, Lawrence Berkeley National Laboratory, 1 Cyclotron Road, 67R5110, Berkeley, CA 94720, phone: 510-486-6640, becohen@lbl.gov, Caroline M. Ajo-Franklin, Department of BioSciences, Rice University, 6100 Main St., MS-140, Houston, TX 77005-1827, phone: 713-348-3497, cajo-franklin@rice.edu.

Author Contributions

The manuscript was written through contributions of all authors. All authors have given approval to the final version of the manuscript.

Supporting Information. Description of supporting information. This material is available free of charge via the Internet at http://pubs.acs.org.

The authors declare no competing financial interest.

This specific, stable, and efficient conjugation of NPs to 2D protein sheets enables the exploration of interactions between pairs of nanoparticles at defined distances for the engineering of protein-based photonic nanomaterials.

Graphical Abstract

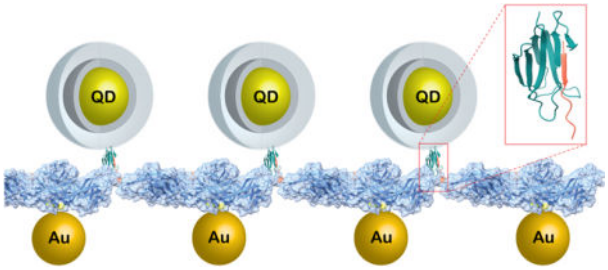

Keywords

S-layer; protein self-assembly; crystalline nanosheets; bioconjugation; quantum dots; upconverting nanoparticles; gold nanoparticles; plasmonics; lifetime imaging

INTRODUCTION

Cells produce protein- and nucleic acid-based assemblies with chemical complexity and structural precision far beyond what is possible with laboratory synthesis or fabrication techniques.[1,2] Controlled patterning of nanoparticles (NPs) along these scaffolds enables the synthesis of complex hybrid materials with potential applications in nanoelectronics, optics, and biochemical sensing.[3–7] Bottom-up approaches using self-assembling DNA- and protein-based scaffolds offer general routes to pattern nanoparticles with some control over spacing and density. For example, DNA origami has been used to scaffold Au into arrays or wires at interparticle distances to allow optical interactions between adjacent AuNPs,[8–10] and disulfides have been engineered into protein tetramers, enabling them to form extended crystalline 2D assemblies able to pattern AuNPs.[11]

While non-covalent self-assembly approaches allow for diverse structures and compositions, they rely on equilibria between assembled and unbound nanoparticles on the larger structure, [8, 9, 12, 13] limiting the efficiency of assembly at low concentrations and the stability of assemblies over longer timescales. For NPs in particular, inherent limits on their concentrations to avoid aggregation (at or below low μM range)[14–16] present challenges for high-density patterning under equilibrium conditions. Appreciable dissociation between building blocks has often limited density of nanoparticle coverage over DNA- or protein-based scaffolds.[17–20] This becomes more limiting as the complexity of the material increases, as decreases in yield may be compounded with each additional building block. For example, engineering plasmonic enhancement of quantum dot (QD) emission with metal NPs requires specific spacing between NPs,[21–23] and low-density labeling of either component creates interparticle distances too large to measure plasmonic effects. For these and other multi-component materials, high-density coverage requires novel and orthogonal methods for linking nanoparticles to scaffolds with no appreciable dissociation.

Protein assemblies are promising scaffolds for the development of hierarchical nanomaterials as they can be engineered with angstrom precision and self-assemble into stable, complex architectures.[1, 24–28] Covalent Au-thiol bonds have been successfully exploited to target AuNPs to Cys side chains,[6, 11, 17, 29] but the intrinsic reactivity and structure encoded within protein assemblies should allow for varied and orthogonal targeting strategies.[30, 31] This richness of protein biochemistry has yet to be exploited to create materials with close and well-defined interactions between different classes of nanoparticles.

Surface layer proteins (S-layers) are found as two-dimensional crystalline arrays on the outer membranes of most prokaryotes. S-layers may be expressed as monomers and will organize into crystalline 2D arrays with well-defined lattice dimensions upon addition of Ca^{2+}.[32, 33] These nanosheets remain stable while floating freely in solution across wide pH and temperature ranges,[34] and can adhere to either wet or dry surfaces,[32] all of which makes them promising for engineering programmable materials. S-layers naturally form 2D rather than 3D crystals, limiting determination of atomic resolution structures by X-ray crystallography,[35, 36] which has presented challenges for engineering many types of S-layer proteins. However, a high-resolution X-ray structure (Figure 1) has been reported for SbsB,[35] the S-layer from thermophile *Geobacillus stearothermophilus*,[37] enabling rational design of SbsB sheets suitable for bioconjugation.[38, 39]

While certain S-layers have been engineered with single nanoparticle attachment sites,[40–42] they have not been explored for the simultaneous display of multiple nanoparticles. High-density attachment of nanoparticles presents added challenges owing to their larger diameters (up to 16 nm in this study), including low dispersibility, limiting possible NP concentrations to orders of magnitude lower than the mM concentrations required for many bimolecular reactions, and potential steric clash between NP at the sheet surface, which should become increasingly problematic as binding sites become occupied and block free NP from accessing vacant sites.

Engineered split proteins SpyTag/Catcher[44] and SnoopTag/Catcher[45] have emerged as robust systems for specific conjugation of materials to proteins.[38, 46, 47] Tag peptides and Catcher proteins bind to one another with nanomolar affinities and self-ligate to form isopeptide bonds (Figure 1C), making them useful for specific and irreversible labeling at low concentrations.[48–50] Leveraging these bioconjugation reactions and Au-thiol binding, here we describe the synthesis of hybrid 2D materials comprising self-assembling S-layer proteins conjugated to pairs of interacting NPs. This approach allows the dense, simultaneous attachment of multiple NP types, with densities up to 30% for SnoopCatcher, about 6-fold higher than AuNPs bonding to Cys clusters. Fluorescence lifetime imaging of SbsB sheets conjugated to both QDs and AuNPs shows shortened radiative decays and brighter fluorescence characteristic of plasmonic enhancement of the QD fluorescence due to short-range interactions between the two species. This work demonstrates efficient conjugation of multiple NPs to specific positions in 2D protein assemblies, which can be generalized to diverse NP types for discovery of protein-based photonic nanomaterials.

MATERIALS AND METHODS

Generation & purification of engineered SbsB proteins.

All plasmids and cell lines are outlined in Table S1. We used Gibson assembly[51] to create a pET28a plasmid (Novagen) that encodes sbsB from *G. stearothermophilus* between NcoI and XhoI sites. The resulting construct contained a C-terminal TEV protease cleavage site followed by a hexa-His tag for purification. The recombinant SbsB variants that contained either SpyTag (AHIVMVDAYKPTK)[44] or SnoopTag (KLGDIEFIKVNK)[45] were preceded or flanked by GSG linkers. For dual labeled sheets, GSG-SpyTag-GSG was inserted either in the mid loop after Asn201 or in the pore loop after Val386, and GSG-SnoopTag was added at the C-terminus after Ser922 (Figure S1). To generate SpyTag, SnoopTag, and tetra-Cys (S662C, T679C, A682C, V698C) SbsB constructs, isolated starter plasmids were subjected to site-directed mutagenesis (Q5 Hot-Start High Fidelity mutagenesis kit, NEB), following the manufacturer's instructions, and mutagenic primers (IDT) (Table S2). Positive clones were confirmed *via* DNA sequencing. Plasmids encoding SbsB variants were transformed into the *E. coli* expression cell line HMS174(DE3) (MilliporeSigma) for heterologous protein expression.

Single colonies from solid media were used to inoculate cultures of LB broth (5 mL) containing kanamycin (50 μg/mL), and grown at 37 °C overnight (250 rpm). This starter culture was then used to inoculate 500 mL LB broth containing kanamycin (50 μg/mL) and grown at 37 °C with shaking (250 rpm). Once cell density reached 0.4 – 0.6 (2 – 4 h post-induction), protein expression was induced with 1 mM IPTG. Cultures were then grown overnight at 18 °C with shaking (250 rpm) to avoid the formation of inclusion bodies. Cells were harvested (6000 × *g*, 20 min, 4 °C) and the cell pellet was resuspended in 30 mL of lysis buffer (20 mM Tris, pH 8.0, 300 mM NaCl, 10 mM imidazole). Cell pellets were stored at − 80 °C. Recombinant His_6-tagged protein was isolated as previously described by gravity-flow immobilized metal-affinity chromatography.[52] Purified protein was then dialyzed against 20 mM Tris pH 8.0 to remove imidazole. All purification steps for the isolation of SbsB Cys cluster, also included 10 mM TCEP, to avoid the formation of disulfide linkages between monomers. A TEV protease cleavage step, to remove the C-terminal His_6-tag, was carried out as previously described[39] and confirmed by SDS-PAGE and Western blot.

Nanosheet formation.

Crystallization of SbsB monomers into nanosheets was triggered by addition of 10 mM $CaCl_2$ to purified SbsB (1–5 mg/mL; 10 – 50 μM) in 20 mM Tris, pH 8.0, with 10 mM TCEP for Cys-containing mutants. The solution was briefly mixed and allowed to sit overnight at room temperature. Protein crystallization was observed as a white solid settled to the bottom of the tube. Nanosheets were stored at 4 °C.

Modification and generation of protein-coupling systems.

Genes encoding for SpyCatcher and SnoopCatcher were encoded within the pDEST14 and pET28A plasmids, respectively (Addgene). Both plasmids also contained an N-terminal His_6 tag for purification purposes, followed by a TEV protease cleavage site. Cys residues were

incorporated into solvent exposed loops of SpyCatcher and SnoopCatcher proteins, specifically at positions S35C and N58C, respectively. Mutagenesis was carried out using a Q5 site-directed mutagenesis kit, per the manufacturer's instructions, using primers shown in Table S2. Cys-containing variants were verified by DNA sequencing. These inserted Cys side chains were required for the attachment of SpyCatcher/SnoopCatcher to the surface of nanoparticles via thiol chemistry.

Plasmids containing our modified SpyCatcher/SnoopCatcher were transformed into BL21(DE3) pLysS *E. coli* cells. Cell growth and recombinant protein expression were carried out following protocols as previously described.[44] Following overnight protein expression, cells were harvested via centrifugation (6000 × *g* for 20 min at 4 °C), The resulting cell pellet was resuspended in 30 mL lysis buffer (20 mM Tris pH 8.0, 300 mM NaCl, 10 mM imidazole) and stored at − 80 °C until further use.

Recombinant His_6-tagged proteins were isolated using a prepacked 1 mL Ni^{2+} column (GE Healthcare). Protein binding was carried out at 10 mM imidazole, followed by wash with 40 mM imidazole for 20 column volumes, and elution at 250 mM imidazole. An additional purification step of preparative SEC was also carried out wherein affinity-purified samples were injected onto Superdex 200 matrix (HiLoad 16/60 column, GE Healthcare) pre-equilibrated with 20 mM Tris pH 8.0, 300 mM NaCl and 10 mM TCEP (for Cys-containing variants). All chromatography steps were conducted at 1 mL/min with an ÄKTA Explorer system (GE Healthcare). Gel filtration confirmed products were a single species with an apparent mass of ~15 kDa. SDS-PAGE analysis further confirmed the solution SEC results, with a single, distinct band for purified Catcher proteins at approximately 15 kDa. Yields for SpyCatcher/SnoopCatcher constructs were typically between 2 – 10 mg/mL.

Nanoparticle synthesis and aqueous passivation.

Yb^{3+}/Er^{3+}-doped $NaYF_4$ and $NaGdF_4$ UCNPs were synthesized following previous methods.[53, 54] For $NaY_{0.78}Yb_{0.2}Er_{0.02}F_4$ UCNPs: to a dry 50-mL round bottom flask, YCl_3 hydrate (0.312 mmol, 95 mg), $YbCl_3$ hexahydrate (0.08 mmol, 31 mg), and $ErCl_3$ hexahydrate (0.008 mmol, 3.1 mg) were added, followed by oleic acid (3.25 g, 10.4 mmol) and 1-octadecene (ODE, 4 mL). The mixture was placed under vacuum, and heated to 110 °C for 1 h, causing the solution to clear. The flask was cooled and filled with N_2, and sodium oleate (1.25 mmol, 381 mg), NH_4F (2 mmol, 74 mg), and ODE (3 mL) were added. The flask was again placed under vacuum and stirred at room temperature for 30 min, and then flushed three times with N_2 filled by vacuum. The reaction was heated to 315 °C, stirred for 45 min under N_2, and then cooled rapidly by a strong stream of air to the outside of the flask following removal of the heating mantle. When the reaction had cooled to 75 °C, ice-cold ethanol (25 mL) was added to precipitate the nanocrystals. The reaction was transferred to a centrifuge tube and centrifuged at 3000 × g for 5 min to precipitate the nanocrystals completely. The supernatant was discarded and the white solid precipitate was resuspended in minimal hexanes (5 mL) to break up the pellet. The nanocrystals were then precipitated again with the addition of ethanol (40 mL) and centrifuged at 3000 × g for 10 min. This resuspension and precipitation were repeated 2 more times. The nanocrystals were resuspended and stored in 10 mL of hexane with 0.1% (*v*/*v*) oleic acid to give a 10 μM

dispersion. $NaGd_{0.78}Yb_{0.2}Er_{0.02}F_4$ UCNPs were synthesized similarly with different proportions of the lanthanide chloride salts.

Hydrophobic UCNPs were transferred to water by encapsulation in poly(*n*-octylacrylamide)-*co*-poly(2-aminoethylacrylamide) (POA, 2.9 kDa) amphiphilic random copolymer.[55] For aqueous dispersion of UCNPs, POA (10 mg, 2.90 μmol) was dissolved in 1 mL of MeOH and 19 mL of $CHCl_3$. UCNPs in hexane (100 μL of 10 μM QDs, 1.0 nmol) were added with stirring, and the solvents were removed under a gentle stream of N_2 overnight. The dry UCNP/polymer residue was then resuspended in 15 mL of 10 mM MES, pH 6.0. This suspension was sonicated for 30 minutes, heated in an 80 °C water bath for 60 minutes, slowly cooled in the bath to room temperature, and then sonicated for 30 minutes. Excess polymer was removed by spin dialysis (Amicon Ultra-15, 50 kDa MWCO), washing with 3 × 15 mL of 10 mM MES, pH 6. The retentate was diluted to 500 μL (2 μM) with MES buffer and centrifuged at 16100 × *g* for 5 min to remove residual polymer and insoluble aggregates. Aqueous UCNP dispersions were stored under ambient conditions.

Hydrophobic CdSe/ZnS QDs with emission maxima of 585 nm (Ocean Nanotech) were transferred to water by encapsulation in amphiphilic copolymer poly(acrylic acid)-*co*-poly(*n*-octylacrylamide)-*co*-poly(2-aminoethylacrylamide) (PAOA, 3 kDa) according to previous studies.[16, 56] For aqueous dispersion of QDs, PAOA (20 mg, 6.25 μmol, 3000-fold excess) was dissolved in 1 mL of MeOH and 19 mL of $CHCl_3$. QDs in hexane (200 μL of 5 μM QDs, 2.0 nmol) were added with stirring, and the solvents were removed under a gentle stream of N_2 overnight. The dry QD/polymer residue was then resuspended in 15 mL of 200 mM sodium bicarbonate buffer, pH 8.0. This suspension was sonicated for 30 minutes, heated in an 80 °C water bath for 60 minutes, slowly cooled in the bath to room temperature, and then sonicated for 30 minutes. Excess polymer was removed by spin dialysis (Amicon Ultra-15, 50 kDa MWCO), washing with 3 × 15 mL of 100 mM HEPES, pH 7.8. The retentate was diluted to 1 mL with HEPES buffer and centrifuged at 16100 × *g* for 5 min to remove residual polymer and insoluble aggregates. Aqueous QD dispersions were stored under ambient conditions.

Nanoparticle-SpyCatcher conjugation.

For QD-SpyCatcher conjugates, PAOA-encapsulated QDs (2 μM, 600 μL) in 100 mM HEPES, pH 7.8, were combined with the crosslinker succinimidyl ester-PEG_2-maleimide ($SM(PEG)_2$, (ThermoFisher, 100 mM, 100 μL) dissolved in DMSO, and mixed at room temperature for 30 min on a rotary mixer. The reaction mixture was diluted to 4 mL with 100 mM HEPES, pH 7.0, and excess PEG reagent was removed by centrifugal dialysis (Amicon Ultra-4, 100 kDa MWCO), washing with 3 × 4 mL of buffer. The retentate was diluted to 500 μL in a 1.5-mL low protein-binding centrifuge tube (Eppendorf), the SpyCatcher Ser35Cys mutant (132 μM, 200 μL) was added, and the reaction was mixed overnight at 4°C on a rotary mixer. The reaction mixture was diluted to 4 mL with 100 mM HEPES, pH 7.0, and excess SpyCatcher protein was removed by centrifugal dialysis (Amicon Ultra-4, 100 kDa MWCO), washing with 4 × 4 mL of buffer. The retentate was diluted to 600 mL in HEPES buffer, and the QD-protein conjugate was stored under ambient conditions.

To generate UCNP-SpyCatcher conjugates, POA-encapsulated UCNPs (10 μM, 200 μL) in 200 mM MES, pH 5.0, were combined with 5,5'-dithiobis(2-nitrobenzoic acid) (Ellman's reagent, 10 mM, 100 μL, Aldrich) and 2-iminothiolane HCl (Traut's reagent, 1 mM, 10 μL, Sigma) dissolved in 100 mM MES, pH 6.0. Under vigorous stirring, 700 μL of 200 mM CAPS buffer, pH 10.0 was added dropwise, and the mixture was allowed to react for 20 mins. The reaction mixture was diluted to 4 mL with 100 mM HEPES, pH 7.5, and excess reagents were removed by centrifugal dialysis (Amicon Ultra-4, 100 kDa MWCO), washing with 3 × 4 mL of HEPES buffer. An aliquot of SpyCatcher S35C protein (200 μM, 100 μL) was desalted on a Bio Spin-6 Column (Bio-rad) and further washed by centrifugal dialysis (Amicon Ultra-4, 3 kDa MWCO), washing with 3 × 4 mL of HEPES buffer to remove all TCEP storage buffer. The retentate was diluted to 100 μL in a 1.5-mL low protein-binding centrifuge tube, the UCNPs were added, and the reaction was mixed overnight at 4 °C on a rotary mixer. The reaction mixture was diluted to 4 mL with 100 mM HEPES, pH 7.5, and excess SpyCatcher protein was removed by centrifugal dialysis (Amicon Ultra-4, 100 kDa MWCO), washing with 4 × 4 mL of buffer. The retentate was diluted to 400 mL in HEPES buffer, and the UCNP-protein conjugate was stored under ambient conditions.

To synthesize AuNP-SpyCatcher conjugates, an aliquot of S35C SpyCatcher (50 μM, 100 μL) was desalted on a Bio Spin-6 Column (Bio-Rad) and further washed by centrifugal dialysis (Amicon Ultra-4, 3 kDa MWCO), washing with 3 × 4 mL of HEPES buffer to remove all TCEP storage buffer. The retained protein was added to 5-nm citrate-coated AuNPs (100 nM, 200 μL, Sigma-Aldrich) in a 1.5-mL low protein-binding centrifuge tube (Eppendorf), and the reaction was gently mixed overnight at 4°C. The reaction mixture was desalted on two consecutive Micro Bio Spin P-30 desalting columns (Bio-Rad, 40 kDa MWCO) to remove any unbound SpyCatcher protein. The AuNPs were diluted to 400 μL in 10 mM HEPES, pH 7.4, and the AuNP-protein conjugate was stored at 4°C.

Nanoparticle characterization.

To determine the size of as-synthesized UCNPs, a dilute dispersion of nanocrystals in hexane was drop cast onto an ultrathin carbon film on lacey carbon support, 400 mesh copper TEM grid (Ted Pella) and dried in a fume hood. Images were collected on a Gemini Ultra-55 Analytical Field Emission Scanning Electron Microscope (Zeiss) in dark-field transmission mode under 30 kV accelerating voltage. Diameters for 100 random particles were manually designated in ImageJ and a distribution was plotted.

To determine the size of aqueous UCNPs and QDs, dispersions were diluted to 20 nM in 100 mM HEPES, pH 7.8 for PAOA-wrapped particles, in 100 mM MES, pH 6.0 for POA-encapsulated NPs, and in 100 mM HEPES, pH 7.0 for SpyCatcher-functionalized nanoparticles. The dispersions were sonicated for 30 minutes prior to measurement. Diameters were measured by dynamic light scattering (DLS) using a Malvern Zetasizer with typical count rates of 150 kilocounts per second. Data were collected for 60 seconds each in 5 separate runs and fit using Malvern Zetasizer software to a volume-weighted size distribution of hydrodynamic diameter. To confirm the stoichiometry of SpyCatcher on the nanoparticle surface, absorption spectra were taken prior to and after conjugation, showing a Trp absorption peak at 280 nm. The concentration of SpyCatcher was determined from this

absorbance and the extinction coefficient (10,810 M^{-1} cm^{-1}), and a ratio with the nanoparticle concentration defined the number of proteins per nanoparticle.

Nanoparticle coupling reactions to SbsB nanosheets.

Crystallized SbsB nanosheets (~1 mg/mL) with the relevant SpyTags or SnoopTags, were incubated in an excess of nanoparticle (1 – 5 μM) functionalized with their relevant protein partner (SpyCatcher/SnoopCatcher). Similarly, AuNPs (5 nm or 100 nm, citrate capped, Sigma) were added in excess for thiol conjugation to Cys-containing SbsB sheets. We found that aggregates were more likely to form when both types of nanoparticles were incubated with nanosheets simultaneously; therefore, sheets were incubated with a single type of nanoparticle at a time. Incubations were carried out overnight at room temperature with gentle rocking. Prior to imaging and further analysis, unbound nanoparticles were removed *via* two centrifugation steps (16000 × *g*, 10 min). The supernatant containing excess nanoparticles, was removed and pelleted sheets were resuspended in 20 mM Tris, pH 8.0.

Confocal microscopy of NP-SbsB nanosheets.

Interference reflection microscopy (IRM) and fluorescence microscopy were carried out on a Zeiss LSM 710 confocal microscope with an Axio Observer.Z1 (Carl Zeiss Micro Imaging). A solution of SbsB nanosheets was mounted between a glass slide and glass coverslips (No. 1.5) using a Secure Seal spacer with a 13 mm diameter, 0.12 mm thickness (ThermoFisher Scientific) and imaged using a 100× oil immersion objective (Plan-Apochromat, 1.40 NA). A 405 nm Ar ion laser was used to excite samples containing QDs and an Arroyo 980 nm continuous wave laser for samples with bound UCNP. To collect reflection images, a 514 nm laser was reflected into the sample using a mBST80/R20 plate. The reflected light was collected and imaged onto the detector. Images were analyzed and exported using Zen Black software.

Scanning transmission electron microscopy (STEM) of SbsB nanosheets.

Engineered SbsB sheets (1 mg/mL) were incubated overnight with 1 – 5 μM NPs. Samples were applied to copper grids with continuous lacey carbon and stained prior to STEM with a methylamine tungstate negative stain (Nano-W). STEM was carried out at 30 kV accelerating voltage. Image analysis and particle counting were carried out in Fiji V1.0.[57] Coverage analysis was performed manually, wherein boxes corresponding to 120 SbsB monomers (100 × 100 nm) were randomly dropped on the image and particles manually counted.

Fluorescence lifetime imaging.

The experimental investigation of lifetime enhancements of the QD- and AuNP-modified sheets were performed using a home-built scanning confocal microscope. Pulsed laser excitation (5 ps pulse width; 40 MHz repetition rate) was provided by a supercontinuum laser source (Leukos) that was filtered using an acousto-optical tunable filter (AOTF; Gooch and Housego) to an ~5 nm-wide band centered at 520 nm. The laser excitation was focused to a diffraction-limited spot (~320 nm in diameter) by a 100× objective with an NA of 0.95 (Nikon). The CW equivalent power for all measurements reported here was ~10 nW. QD

emission from the diffraction-limited excitation spot was collected by the same objective, passed through two 532 nm long-pass filters (Semrock) and focused on a single-photon counting avalanche photodiode (SC-APD; MPD) for lifetime measurements or a spectrometer (Andor) connected to a cooled scientific charge coupled device (CCD; Andor iXon) for emission spectra measurements. For the lifetime measurements, time-correlated single photon counting (TCSPC) was performed using a PicoHarp device. All transients reported in this work are significantly longer than the instrument response which exhibited a nominal full-width-at-half-maximum of ~70 ps. To simplify lifetime comparisons, we calculated the effective lifetime of each trace, τ_{eff}, as calculated by:

$$\tau_{\text{eff}} = \frac{\sum A_i \tau_i}{\sum A_i}.$$

where A_i are weighting factors and τ_i are lifetimes obtained from decay curve fittings.

RESULTS

Conjugation of AuNP to S-layer nanosheets.

To conjugate different types of nanoparticles to S-layer nanosheets, we first leveraged the strength of Au-thiol bonds[58] and introduced a cluster of Cys residues in the SbsB monomer to produce an AuNP binding domain (Figures 1 and S1). Targeted residues were identified from the SbsB structure (Figure 1A) and by identifying solvent-exposed side chains in the lattice.[35, 59] Four residues (Ser662, Thr679, Ala682, Val698) that form a ~10 × 10 Å square (Figure 1B) on the outward facing surface of SbsB were substituted with Cys to form a solvent-exposed thiol cluster. Assembly of Cys-enriched SbsB nanosheets from monomers (Figure S2) was triggered by addition of Ca^{2+} (refs. 32, 33) and characterized by scanning transmission electron microscopy (STEM) and interference reflection microscopy (IRM), showing that Cys-modified sheets have lattice dimensions and sizing (typically rectangular, ranging from 1 – 10 μm in length) similar to wild-type sheets (Figures 2, S3). To probe metallic nanoparticle conjugation, we incubated unmodified sheets or tetra-Cys sheets with citrate-capped 5 nm AuNPs and analyzed the reaction by STEM. We chose 5-nm AuNPs because they fit within the SbsB nanosheet lattice spacing of 8 × 11 nm,[35] but are large enough to be imaged and show measurable plasmonic effects (described below). SbsB nanosheets incorporating the tetra-Cys cluster, but not native SbsB nanosheets, show AuNP binding (Figure 2B), with an overall sheet coverage of ~5 %. Even with optimized conditions, we see that the Cys clusters are able bind metallic NPs at modest efficiency and poor uniformity across the nanosheet. All attempts to label SbsB monomers with AuNPs before nanosheet crystallization led to intractable aggregates, likely owing to the capacity of each AuNP to conjugate multiple SbsB monomers and the strong tendency of those monomers to crystallize.[33, 38]

Conjugation of diverse nanoparticles using self-ligating proteins.

To improve labeling efficiency of NPs to nanosheets, we examined whether the self-ligating split proteins SpyTag/SpyCatcher and SnoopTag/SnoopCatcher could selectively conjugate NPs to SbsB arrays more effectively than Cys clusters. While SpyTag 13mer peptides have

been shown to conjugate at both internal and terminal positions, we chose the unstructured C-terminal tail of SbsB for SpyTag insertion because of its apparent unimportance in SbsB folding and assembly.[35] SbsB C-SpyTag constructs were expressed at similar levels as wild type SbsB (Figure S2), and STEM reveals highly ordered sheets similar to wild-type, indicating the 13-amino acid peptide does not hinder biosynthesis or assembly into crystalline arrays (Figure S2). In SbsB sheets, SpyTag peptides are accessible to SpyCatcher, as seen in a time series followed by SDS-PAGE, with the appearance of a 110 kDa band corresponding to the SpyCatcher-SbsB C-SpyTag conjugate (Figure S4). A significant fraction of sites in the sheet remain unconjugated after an 18 h exposure to excess SpyCatcher, consistent with kinetic studies showing these reactions do not go to completion.[44, 50] Previous work with other S-layer fusions[39] has shown up to 5-fold changes SpyCatcher-SpyTag conjugation efficiency depending on where the SpyTag is incorporated in the S-layer.

We next probed whether the SpyTag/Catcher system could enable high-density attachment of inorganic nanocrystals, using either semiconductor quantum dots (QDs)[16, 60] or lanthanide-doped $NaYF_4$ upconverting nanoparticles (UCNPs)[53, 55] doped with 20% Yb^{3+} and 2% Er^{3+}. Hydrophobic inorganic nanocrystals were synthesized by colloidal methods and characterized by TEM and luminescence.[16, 53] To impart colloidal stability and resistance to aggregation in aqueous media, both types of nanocrystals were encapsulated in amphiphilic copolymers bearing surface amines as bioconjugation handles.[55, 56, 61] Aqueous NP sizes and dispersity were measured by dynamic light scattering (DLS), showing no aggregation and hydrodynamic diameters of 11, 13, and 16 nm for CdSe/ZnS QDs, $NaGdF_4$ UCNPs, and $NaYF_4$ UCNPs, respectively (Figure S5). To functionalize these NPs for conjugation to SbsB-SpyTag sheets, a single Cys at Ser35 was introduced in a SpyCatcher loop, expressed, and purified. For Cys-mediated attachment, amines on the NP surface were converted to Cys-reactive groups either with amine-thiol heterobifunctional crosslinkers or by sequential treatment with Traut's and Ellman's reagents (Figure S6). Trp fluorescence shows a stoichiometry of 10–30 surface SpyCatcher proteins per NP, depending on NP size, and these conjugates remained dispersed in buffer with little apparent aggregation (Figure S5). Attempts to display SpyTag peptides on nanocrystal surfaces led to complete aggregation, even with sparse surface display, likely owing to peptide hydrophobicity.

The SpyCatcher-functionalized QDs were incubated with SbsB C-SpyTag sheets (Figure 2C) for covalent attachment and then characterized by STEM and confocal microscopy. Nanoparticle-conjugated SpyCatcher maintained its reactivity with SpyTag, resulting in specific conjugation to tagged SbsB nanosheets. QDs were readily imaged bound to nanosheets via STEM (Figure 2C), with NPs occupying 18% of possible SpyTag attachment sites. Confocal images of QD-conjugated sheets show emission localized to sheets (Figure 2G–I) with a characteristic emission peak at 585 nm.

A second self-ligating split protein, SnoopTag/Catcher,[45] was investigated for NP-SbsB sheet conjugation and whether it can be used selectively in the presence of SpyTag/Catcher. The SnoopTag 12mer was engineered into the C-terminus of SbsB and incubated with SnoopCatcher-conjugated UCNPs (Figure 3A). Similar to SpyTag, STEM images show SnoopTag has no appreciable effect on the SbsB lattice dimensions or sheet size (Figure 3).

SnoopCatcher-conjugated UCNPs show significantly higher conjugation to nanosheets compared to their SpyCatcher counterparts, with 13-nm UCNPs coupling efficiency increasing from 10.7 ± 0.9% to 17.4 ± 0.9% and 16-nm UCNPs from 2.4 ± 0.4% to 30.6 ± 2.0% (Figure 4). SpyCatcher-coated AuNPs also show a marginally improved labeling efficiency compared to citrate-coated AuNPs targeted to the Cys cluster. STEM images reveal uniform nanoparticle binding to sheets for both 16-nm $NaYF_4$ UCNPs and 13-nm $NaGdF_4$ UCNPs (Figure 3). When UCNP-conjugated sheets are excited at 980 nm, characteristic upconverted Er^{3+} emission peaks at 545 and 660 nm are localized to SbsB sheet region with no measurable off-sheet emission (Figure 3C–H). Taken together, these Spy- and Snoop-Catcher experiments demonstrate more efficient labeling than seen with multivalent Cys binding to AuNP.

Simultaneous attachment of different NP to SbsB nanosheets.

To introduce 2 distinct attachment sites in SbsB for simultaneous labeling, we targeted two loop regions in addition to the C-terminus (Figure S7). The mid loop (ML) lies between the sugar-binding domain and crystallization domain of full-length SbsB and the pore loop (PL) lies between domains III and IV and spans the inter-monomer pore. All modifications, including dual tagged constructs, result in crystalline nanosheets similar to wild type sheets upon the addition of Ca^{2+}. Based on expression and assembly efficiency, 2 dual-modified SbsB variants were investigated to determine their ability to selectively conjugate distinct nanoparticles: SbsB mid loop (ML) with SpyTag C-terminal SnoopTag, and SbsB pore loop (PL) SpyTag with C-terminal SnoopTag. Dual-labeled

SbsB nanosheets display the capacity to conjugate both QDs and UCNPs sequentially through purified single-Cys SpyCatcher or SnoopCatcher conjugated to NP surfaces (Figures 1,5 and Methods). Ionic strength, added detergents, order of addition, and sonication were tested to optimize reactions for disperse, high-density coverage (Figure S8). Sequential addition of NPs proved essential, as did high salt (500 mM NaCl), which may reduce NP aggregation or increase effective concentration of NPs near the sheets by electrostatic screening. We note that SbsB sheets and NPs proved resistant to low concentrations of detergent (0.5 – 1% Tween or SDS), although sonication resulted in aggregation of NP, possibly due to irreversible denaturation of SpyCatcher or SnoopCatcher on the NP surface. To synthesize novel 2D materials with interacting NPs, we added both AuNPs and QD-SpyCatcher to SbsB sheets bearing both Cys clusters and C-SpyTag peptides (Figure 6A,B). Despite some clustering of NPs (Figure S8), we observe multiple regions of colocalization, with different NP types within 10 nm of one another.

Plasmonic interactions between NP on SbsB nanosheets.

To study colocalization of 2 different NPs on a 2D protein sheet, we measured the interactions between QDs and AuNP by fluorescence lifetime imaging. We sought to determine if conjugated NP are sufficiently close (ca. 2–20 nm)[21, 23, 62] for the QD emission to show significant coupling to neighboring AuNPs, as STEM images show heterogeneous distributions in dual-labeled nanosheets (Figure S8A). First, we compared the excited state relaxation dynamics of the QDs acquired from 65×65 μm^2 areas of QD-only and QD- and AuNP-conjugated protein sheets dispersed on a glass substrate (Figure 6A). The large area

measurements provide ensemble averages of many individual protein sheets, as well as of areas of NP heterogeneity within dual-labeled sheets (Figure 5A). Because the fluorescent transients cannot be fit to single exponential decays, we calculated effective lifetimes (τ_{eff}) from biexponential fittings to simplify comparisons (Methods and Table S3). Addition of AuNPs to QD-conjugated sheets reduces τ_{eff} values from 8.4 ns to 4.6 ns (Figure 6A), a significant decrease consistent with close interparticle spacing needed for plasmonic coupling between the AuNPs and QDs.

We also examined the spatial heterogeneity of QD fluorescence in both sets of NP-labeled protein sheets. While the QD-only protein sheets show no significant spatial heterogeneity in brightness or lifetimes, sheets with both QDs and AuNPs have regions of varying QD brightness (Figure 6). Steady-state emission peaks and lineshapes of the brighter regions are indistinguishable from those acquired from dimmer regions (Figure 6B). By contrast, the areas with brighter emission exhibit substantially faster decay dynamics (τ_{eff} = 1.5 ns; Figure 6C) than areas with dimmer emission (τ_{eff} = 6.4 ns; Figure 6D). The combined observation of brighter emission with decreased excited state lifetime indicates that in specific regions of the sample, AuNP enhance the fluorescence of the QDs, likely by increasing both the radiative and excitation rates. Localized regions of highest enhancement and fastest relaxation dynamics are typically 2-4-fold brighter than the corresponding regions with unperturbed lifetimes in the dual-modified sheets. The fastest measured τ_{eff} (Figure 6C) is >5-fold faster than in the protein sheets with QDs alone.

Nanosheets containing only Cys-conjugated AuNPs exhibit a weak, broad emission with a shorter lifetime than the QDs alone (Figure S9), characteristic of the weak fluorescence sometimes observed from AuNPs.[63] Although this broad emission overlaps with the QD emission, it is at least an order of magnitude weaker than QD emission, so this background signal does not significantly alter analysis of either steady-state or lifetime data. Taken together, the AuNP-QD sheets exhibit shortened lifetimes and spatial heterogeneity in both brightness and lifetime, indicating some QDs are spaced close enough to neighboring AuNPs to be plasmonically coupled.

DISCUSSION

Cells synthesize materials of unrivaled order and complexity, including 2-dimensional materials that can serve as starting points for exploring hybrid materials with novel optical, electronic, and sensing properties. S-layer proteins form stable, micron-sized nanosheets that serve as protective layers around prokaryotes, archaea, and a few eukaryotes, and these precise periodic 2D structures may serve as scaffolds for ordered hybrid materials. Crystalline SbsB sheets have a consistent 3.5-nm thickness with less roughness and fewer defects compared to fabricated nanofilms,[64] are robust across a range of solution conditions, and require just Ca^{2+} to trigger assembly of micron scale 2D structures in water. But significant challenges remain to realize the potential of these and other biomolecules as nanoparticle scaffolds, including: high-density attachment of NPs across polymeric structures, formation of irreversible bonds with NPs, generally applicable attachment of NPs with diverse chemistries, and simultaneous attachment of multiple types of NPs to a single structure. Compared to labeling protein complexes with small molecules, reactions between

nanoparticles and protein complexes are constrained by possible steric clash and by inherent limits on NP concentration that prohibit reactions from being driven to completion by simply increasing the concentration of a reactant.

NP labeling efficiency of SbsB sheets varies with conjugation method (thiol-Au *versus* isopeptide bond formation), coupling system, and NP size (Figure 4). We observe that Au-thiol bond formation is the least efficient route for NP conjugation, even with structure-guided design of a tetravalent Cys cluster (Figure 1B). This difference may arise from the energetics of bond formation and dissociation, as amide bonds (~200 kcal/mol) are stronger than Au-thiol bonds (20 – 60 kcal/mol).[58] While 4 Cys are displayed in each SbsB subunit, it is unknown whether all thiols are presented in a geometry that would allow simultaneous contacts with the AuNP. We also observe that the SnoopTag/Catcher system is more efficient than SpyTag/Catcher for conjugation to SbsB for all nanoparticles tested, with 16-nm UCNPs showing the most significant differences (Figure 4). This observation is notable in that the split self-ligating proteins are engineered from paralogous genes,[44, 45] suggesting that reaction differences are due to other factors such as accessibility of the peptidyl tags on the nanosheet surface. SnoopTag (KLGDIEFIKVNK) has 3 more charged sidechains around its isopeptide-forming Asn than SpyTag (AHIVMVDAYKPTK) has surrounding its reactive Asp, which may allow SnoopTag to extend away from the protein sheet into solution more readily. Recently optimized SpyTag/Catcher sequences also contain added charges in the peptide and have shown faster kinetics with more complete reactions at low concentrations,[50] and these may be useful for high-efficiency nanosheet labeling. Charged linkers around the Tag sequences may also improve their reactivity, although these could be constrained by protein folding and assembly requirements. Differences in labeling efficiency between UCNPs and QDs may arise from varying NP surface charge, as the surface polymers on UCNPs have much more positive zeta potentials than those passivating the QDs.[55, 56]

Interactions between NPs and between NPs and SbsB nanosheets are governed by a series of competing forces[65, 66] that can be used to understand the heterogeneous conjugation patterns seen here (Figures 2,3,5). van der Waals interactions between large (>10 nm) colloidal NPs in water are strongly attractive at close range, while electrostatic double layer forces are repulsive and fall off at distances past the Debye length. Added electrolytes, such as the 500 mM NaCl used in optimized SpyCatcher or SnoopCatcher reactions, screen these repulsive forces between charged NPs, so that attractive forces dominate. The observed NP clusters may arise from van der Waals forces between free NPs and NPs conjugated to sheets, so that an initial NP-nanosheet conjugation will seed conjugations at neighboring SbsB sites. Loosely held NP aggregates may also create high effective concentrations of NPs at the nanosheet surface, leading to the observed clustering. Both of these scenarios are likely to be enhanced by attractive van der Waals interactions between NPs and the nanosheets themselves. These attractive forces may be counterbalanced by steric clash between free NPs and NPs conjugated to nanosheets, which might impede access to free SpyTag or SnoopTag sites. In addition, because the NP are multivalent—each displaying between 10–30 surface SpyCatcher or SnoopCatcher proteins—a single NP may form bonds with multiple neighboring SbsB sites. This would lead to NP with fewer immediate neighbors, rather than the clustering that is observed, suggesting that NP and nanosheet geometries do not align to permit bonds from neighboring SbsB monomers to a single NP.

Pairing either SpyTag with SnoopTag (Figure 5) or SpyTag with a Cys cluster allows for the conjugation of multiple NP types to single SbsB monomers within the 2D sheet. Combining a C-terminal SpyTag with an internal Cys cluster allows conjugation of AuNPs and QDs on opposite faces of the protein (Figure 1A). We observe shortened radiative decays and increased brightness for QDs on sheets also labeled with AuNPs (Figure 6 and Table S1), consistent with coupling of the QD with the electromagnetic environment of the AuNP.[23] This decrease of the QD excited state lifetime, which is accompanied by an increase in emission intensity, may be attributed to plasmonic enhancement *via* increased excitation rates and the Purcell effect.[21–23] Measured spatial variation in QD radiative decays within a single nanosheet (Figure 6C, D) is evidence that electronic interactions between QDs and AuNPs are not homogeneous owing to variation in interparticle distances. STEM measurements (Figure S3) and X-ray structures of the SbsB monomer[35] bear this out, as AuNPs and QDs conjugated to opposite faces of the same monomer are separated by ~7 nm edge-to-edge distance, as close as ~3 nm for neighboring monomers, to larger separations along the structure.

It is noteworthy that NPs with fundamentally different inorganic chemistries (semiconductor CdSe/ZnS *versus* lanthanide-doped metal fluorides) can be coupled to proteins with either Spy- or SnoopCatcher systems. This indifference to NP chemistry arises from the amphiphilic polymers that passivate hydrophobic NP without regard to their inorganic cores, [14, 16, 61] and are typically needed to preserve bright emission in aqueous media.[56, 67, 68] This contrasts with metal-thiol bonds, which are specific to metal NP and do not appreciably change the optoelectronic properties of the NP. Amphiphilic polymer passivation and bioconjugation to protein sheet may be extended to other classes of NPs with interesting optical properties, such as nanodiamonds,[14] perovskites,[69] and photon avalanching NPs.[70] Further iterations of these materials could also extend into other protein-assembly geometries, such as 3D lamellar structures.[39]

CONCLUSIONS

We have demonstrated that SbsB nanosheets are versatile scaffolds for the high-density conjugation of AuNPs, QDs, and UCNPs to synthesize 2D materials incorporating multiple types of NPs. SbsB monomers are amenable to a range of mutations while maintaining their ability to crystallize into large, regular 2D nanomaterials, and Spy- and SnoopCatcher systems enable orthogonal stable conjugation of varying NPs. Combined with thiol-Au coupling, dual modification of protein sheets can colocalize NPs to produce plasmonic coupling between AuNP and QDs. This modular synthesis may be extended to a variety of inorganic nanocrystals for discovery of stable, hybrid 2D materials with interesting and unusual optoelectronic properties.

Supplementary Material

Refer to Web version on PubMed Central for supplementary material.

ACKNOWLEDGEMENTS

We thank Cheryl Tajon for help with UCNP synthesis and passivation, Behzad Rad for help with protein expression and assembly, and Paul Ashby for comments on the manuscript. This work was supported by National Institutes of Health award R01NS096317 (B.E.C.) and the Defense Advanced Research Projects Agency (Engineered Living Materials Program, C.M.A-F.). Work at the Molecular Foundry was supported by the Director, Office of Science, Office of Basic Energy Sciences, Division of Materials Sciences and Engineering, of the U.S. Department of Energy under Contract No. DE-AC02-05CH11231.

Funding Sources

National Institutes of Health

Defense Advanced Research Projects Agency

REFERENCES

1]. Hamley IW (2019) Protein Assemblies: Nature-Inspired and Designed Nanostructures. Biomacromolecules 20, 1829–1848. DOI: 10.1021/acs.biomac.9b00228 [PubMed: 30912925]

[2]. Pieters BJGE, van Eldijk MB, Nolte RJM, and Mecinović J (2016) Natural supramolecular protein assemblies. Chem. Soc. Rev 45, 24–39. DOI: 10.1039/C5CS00157A [PubMed: 26497225]

[3]. Shipway AN, Katz E, and Willner I (2000) Nanoparticle arrays on surfaces for electronic, optical, and sensor applications. Chemphyschem 1, 18–52. DOI: 10.1002/1439-7641(20000804)1:1<18::AID-CPHC18>3.0.CO;2-L [PubMed: 23696260]

[4]. Sun J, Wang Y, and Liao J (2018) Tailoring two-dimensional nanoparticle arrays into various patterns, Nanotechnology 29, 044003. DOI: 10.1088/1361-6528/aa9ab3 [PubMed: 29135459]

[5]. Tian L, Luan J, Liu K-K, Jiang Q, Tadepalli S, Gupta MK, Naik RR, and Singamaneni S (2016) Plasmonic Biofoam: A Versatile Optically Active Material. Nano Lett. 16, 609–616. DOI: 10.1021/acs.nanolett.5b04320 [PubMed: 26630376]

[6]. Zhang J, Zhou K, Zhang Y, Du M, and Wang Q (2019) Precise Self-Assembly of Nanoparticles into Ordered Nanoarchitectures Directed by Tobacco Mosaic Virus Coat Protein. Advanced Materials 31, 1901485. DOI: 10.1002/adma.201901485

[7]. Zhou K, Zhang J, and Wang Q (2015) Site-Selective Nucleation and Controlled Growth of Gold Nanostructures in Tobacco Mosaic Virus Nanotubulars. Small 11, 2505–2509. DOI: 10.1002/smll.201401512 [PubMed: 25612918]

[8]. Kuzyk A, Schreiber R, Fan Z, Pardatscher G, Roller E-M, Högele A, Simmel FC, Govorov AO, and Liedl T (2012) DNA-based self-assembly of chiral plasmonic nanostructures with tailored optical response. Nature 483, 311–314. DOI: 10.1038/nature10889 [PubMed: 22422265]

[9]. Roller E-M, Besteiro LV, Pupp C, Khorashad LK, Govorov AO, and Liedl T (2017) Hotspot-mediated non-dissipative and ultrafast plasmon passage. Nat. Phys 13, 761–765. DOI: 10.1038/nphys4120 [PubMed: 28781603]

[10]. Zheng J, Constantinou PE, Micheel C, Alivisatos AP, Kiehl RA, and Seeman NC (2006) Two-dimensional nanoparticle arrays show the organizational power of robust DNA motifs. Nano Lett. 6, 1502–1504. DOI: 10.1021/nl060994c [PubMed: 16834438]

[11]. Du M, Zhou K, Wang X, Zhang J, Zhang Y, Dong J, Wu L, Qiao Z, Chen G, and Wang Q (2020) Precise Fabrication of De Novo Nanoparticle Lattices on Dynamic 2D Protein Crystalline Lattices. Nano Lett. 20, 1154–1160. DOI: 10.1021/acs.nanolett.9b04574 [PubMed: 31874042]

[12]. Lee J, Huh J-H, Kim K, and Lee S (2018) DNA Origami-Guided Assembly of the Roundest 60--100 nm Gold Nanospheres into Plasmonic Metamolecules. Adv. Funct. Mater 28, 1707309. DOI: 10.1002/adfm.201707309

[13]. Liu N, and Liedl T (2018) DNA-Assembled Advanced Plasmonic Architectures. Chem. Rev 118, 3032–3053. DOI: 10.1021/acs.chemrev.7b00225 [PubMed: 29384370]

[14]. Bumb A, Sarkar SK, Billington N, Brechbiel MW, and Neuman KC (2013) Silica encapsulation of fluorescent nanodiamonds for colloidal stability and facile surface functionalization. J. Am. Chem. Soc 135, 7815–7818. DOI: 10.1021/ja4016815 [PubMed: 23581827]

[15]. Kim T, Lee K, Gong M-S, and Joo S-W (2005) Control of Gold Nanoparticle Aggregates by Manipulation of Interparticle Interaction. Langmuir 21, 9524–9528. DOI: 10.1021/la0504560 [PubMed: 16207031]

[16]. Wichner SM, Mann VR, Powers AS, Segal MA, Mir M, Bandaria JN, DeWitt MA, Darzacq X, Yildiz A, and Cohen BE (2017) Covalent Protein Labeling and Improved Single-Molecule Optical Properties of Aqueous CdSe/CdS Quantum Dots. ACS Nano 11, 6773–6781. DOI: 10.1021/acsnano.7b01470 [PubMed: 28618223]

[17]. Badelt-Lichtblau H, Kainz B, Völlenkle C, Egelseer E-M, Sleytr UB, Pum D, and Ilk N (2009) Genetic engineering of the S-layer protein SbpA of Lysinibacillus sphaericus CCM 2177 for the generation of functionalized nanoarrays. Bioconjug. Chem 20, 895–903. DOI: 10.1021/bc800445r [PubMed: 19402706]

[18]. Johnson-Buck A, Nangreave J, Jiang S, Yan H, and Walter NG (2013) Multifactorial Modulation of Binding and Dissociation Kinetics on Two-Dimensional DNA Nanostructures. Nano Lett 13, 2754–2759. DOI: 10.1021/nl400976s [PubMed: 23701430]

[19]. Mathur D, Klein WP, Chiriboga M, Bui H, Oh E, Nita R, Naciri J, Johns P, Fontana J, Díaz SA, and Medintz IL (2019) Analyzing fidelity and reproducibility of DNA templated plasmonic nanostructures. Nanoscale 11, 20693–20706. DOI: 10.1039/C9NR03711J [PubMed: 31642466]

[20]. Thomas A, Matthaei JF, and Baneyx F (2018) A Self-Assembling Two-Dimensional Protein Array is a Versatile Platform for the Assembly of Multicomponent Nanostructures. Biotechnol. J 13, e1800141. DOI: 10.1002/biot.201800141 [PubMed: 30168658]

[21]. Bardhan R, Grady NK, Cole JR, Joshi A, and Halas NJ (2009) Fluorescence enhancement by Au nanostructures: nanoshells and nanorods. ACS Nano 3, 744–752. DOI: 10.1021/nn900001q [PubMed: 19231823]

[22]. Ratchford D, Shafiei F, Kim S, Gray SK, and Li X (2011) Manipulating coupling between a single semiconductor quantum dot and single gold nanoparticle. Nano Lett 11, 1049–1054. DOI: 10.1021/nl103906f [PubMed: 21280639]

[23]. Tam F, Goodrich GP, Johnson BR, and Halas NJ (2007) Plasmonic enhancement of molecular fluorescence. Nano Lett 7, 496–501. DOI: 10.1021/nl062901x [PubMed: 17256995]

[24]. Azam A, and Tullman-Ercek D (2016) Type-III secretion filaments as scaffolds for inorganic nanostructures. J. R. Soc. Interface 13, 20150938. DOI: 10.1098/rsif.2015.0938 [PubMed: 26763334]

[25]. Botyanszki Z, Tay PKR, Nguyen PQ, Nussbaumer MG, and Joshi NS (2015) Engineered catalytic biofilms: Site-specific enzyme immobilization onto E. coli curli nanofibers. Biotechnol. Bioeng 112, 2016–2024. DOI: 10.1002/bit.25638 [PubMed: 25950512]

[26]. Hong SH, Hegde M, Kim J, Wang X, Jayaraman A, and Wood TK (2012) Synthetic quorum-sensing circuit to control consortial biofilm formation and dispersal in a microfluidic device. Nat. Commun 3, 613. DOI: 10.1038/ncomms1616 [PubMed: 22215088]

[27]. Luo Q, Hou C, Bai Y, Wang R, and Liu J (2016) Protein Assembly: Versatile Approaches to Construct Highly Ordered Nanostructures. Chem. Rev 116, 13571–13632. DOI: 10.1021/acs.chemrev.6b00228 [PubMed: 27587089]

[28]. Subramanian RH, Suzuki Y, Tallorin L, Sahu S, Thompson M, Gianneschi NC, Burkart MD, and Tezcan FA (2020) Enzyme-Directed Functionalization of Designed, Two-Dimensional Protein Lattices. Biochemistry Article ASAP. DOI: 10.1021/acs.biochem.0c00363.

[29]. Jung J, Lakatos M, Bengs S, Matys S, Raff J, Blüher A, and Cuniberti G (2019) S-layer protein-AuNP systems for the colorimetric detection of metal and metalloid ions in water. Colloids Surf. B Biointerfaces 183, 110284. DOI: 10.1016/j.colsurfb.2019.06.014 [PubMed: 31421406]

[30]. Höller RPM, Dulle M, Thomä S, Mayer M, Steiner AM, Förster S, Fery A, Kuttner C, and Chanana M (2016) Protein-Assisted Assembly of Modular 3D Plasmonic Raspberry-like Core/Satellite Nanoclusters: Correlation of Structure and Optical Properties. ACS Nano 10, 5740–5750. DOI: 10.1021/acsnano.5b07533 [PubMed: 26982386]

[31]. McMillan RA, Paavola CD, Howard J, Chan SL, Zaluzec NJ, and Trent JD (2002) Ordered nanoparticle arrays formed on engineered chaperonin protein templates. Nat. Mater 1, 247–252. DOI: 10.1038/nmat775 [PubMed: 12618787]

[32]. Chung S, Shin S-H, Bertozzi CR, and De Yoreo JJ (2010) Self-catalyzed growth of S layers via an amorphous-to-crystalline transition limited by folding kinetics. Proc. Natl. Acad. Sci. U. S. A 107, 16536–16541. DOI: 10.1073/pnas.1008280107 [PubMed: 20823255]

[33]. Rad B, Haxton TK, Shon A, Shin S-H, Whitelam S, and Ajo-Franklin CM (2015) Ion-specific control of the self-assembly dynamics of a nanostructured protein lattice. ACS Nano 9, 180–190. DOI: 10.1021/nn502992x [PubMed: 25494454]

[34]. Engelhardt H, and Peters J (1998) Structural Research on Surface Layers: A Focus on Stability, Surface Layer Homology Domains, and Surface Layer–Cell Wall Interactions. J. Struct. Biol 124, 276–302. DOI: 10.1006/jsbi.1998.4070 [PubMed: 10049812]

[35]. Baranova E, Fronzes R, Garcia-Pino A, Van Gerven N, Papapostolou D, Péhau-Arnaudet G, Pardon E, Steyaert J, Howorka S, and Remaut H (2012) SbsB structure and lattice reconstruction unveil Ca2+ triggered S-layer assembly. Nature 487, 119–122. DOI: 10.1038/nature11155 [PubMed: 22722836]

[36]. Bharat TAM, Kureisaite-Ciziene D, Hardy GG, Yu EW, Devant JM, Hagen WJH, Brun YV, Briggs JAG, and Löwe J (2017) Structure of the hexagonal surface layer on Caulobacter crescentus cells. Nat Microbiol 2, 17059. DOI: 10.1038/nmicrobiol.2017.59 [PubMed: 28418382]

[37]. Sleytr UB, and Sára M (1997) Bacterial and archaeal S-layer proteins: structure-function relationships and their biotechnological applications. Trends Biotechnol. 15, 20–26. DOI: 10.1016/S0167-7799(96)10063-9 [PubMed: 9032989]

[38]. Charrier M, Li D, Mann V, Yun L, Jani S, Rad B, Cohen BE, Ashby PD, Ryan K, and Ajo-Franklin CM (2018) Engineering the S-layer of Caulobacter crescentus as a Foundation for Stable, High-Density, 2D Living Materials. ACS Synth. Biol 8, 181–190. DOI: 10.1021/acssynbio.8b00448

[39]. Manea F, Garda VG, Rad B, and Ajo-Franklin CM (2020) Programmable assembly of 2D crystalline protein arrays into covalently stacked 3D bionanomaterials. Biotechnol. Bioeng 117, 912–923. DOI: 10.1002/bit.27261 [PubMed: 31885073]

[40]. Hall SR, Shenton W, Engelhardt H, and Mann S (2001) Site-specific organization of gold nanoparticles by biomolecular templating. Chemphyschem 2, 184–186. DOI: 10.1002/1439-7641(20010316)2:3<184::AID-CPHC184>3.0.CO;2-J [PubMed: 23696461]

[41]. Mark SS, Bergkvist M, Yang X, Teixeira LM, Bhatnagar P, Angert ER, and Batt CA (2006) Bionanofabrication of metallic and semiconductor nanoparticle arrays using S-layer protein lattices with different lateral spacings and geometries. Langmuir 22, 3763–3774. DOI: 10.1021/la053115v [PubMed: 16584254]

[42]. Shenton W, Pum D, Sleytr UB, and Mann S (1997) Synthesis of cadmium sulphide superlattices using self-assembled bacterial S-layers. Nature 389, 585–587. DOI: 10.1038/39287

[43]. Li L, Fierer JO, Rapoport TA, and Howarth M (2014) Structural analysis and optimization of the covalent association between SpyCatcher and a peptide Tag. J. Mol. Biol 426, 309–317. DOI: 10.1016/j.jmb.2013.10.021 [PubMed: 24161952]

[44]. Zakeri B, Fierer JO, Celik E, Chittock EC, Schwarz-Linek U, Moy VT, and Howarth M (2012) Peptide tag forming a rapid covalent bond to a protein, through engineering a bacterial adhesin. Proc. Natl. Acad. Sci. U. S. A 109, E690–E697. DOI: 10.1073/pnas.1115485109 [PubMed: 22366317]

[45]. Veggiani G, Nakamura T, Brenner MD, Gayet RV, Yan J, Robinson CV, and Howarth M (2016) Programmable polyproteams built using twin peptide superglues. Proc. Natl. Acad. Sci. U. S. A 113, 1202–1207. DOI: 10.1073/pnas.1519214113 [PubMed: 26787909]

[46]. Fairhead M, Veggiani G, Lever M, Yan J, Mesner D, Robinson CV, Dushek O, van der Merwe PA, and Howarth M (2014) SpyAvidin hubs enable precise and ultrastable orthogonal nanoassembly. J. Am. Chem. Soc 136, 12355–12363. DOI: 10.1021/ja505584f [PubMed: 25111182]

[47]. Pessino V, Citron YR, Feng S, and Huang B (2017) Covalent Protein Labeling by SpyTag-SpyCatcher in Fixed Cells for Super-Resolution Microscopy. Chembiochem 18, 1492–1495. DOI: 10.1002/cbic.201700177 [PubMed: 28514494]

[48]. Anuar INAK, Khairil IN, Banerjee A, Keeble AH, Carella A, Nikov GI, and Howarth M (2019) Spy&Go purification of SpyTag-proteins using pseudo-SpyCatcher to access an oligomerization toolbox. Nat. Commun 10, 1734. DOI: 10.1038/s41467-019-09678-w [PubMed: 30988307]

[49]. Bedbrook CN, Kato M, Ravindra Kumar S, Lakshmanan A, Nath RD, Sun F, Sternberg PW, Arnold FH, and Gradinaru V (2015) Genetically Encoded Spy Peptide Fusion System to Detect Plasma Membrane-Localized Proteins In Vivo. Chem. Biol 22, 1108–1121. DOI: 10.1016/j.chembiol.2015.06.020 [PubMed: 26211362]

[50]. Keeble AH, Turkki P, Stokes S, Khairil IN, Rahikainen R, Hytönen VP, and Howarth M (2019) Approaching infinite affinity through engineering of peptide–protein interaction, Proc. Natl. Acad. Sci. U. S. A 116, 26523–26533. DOI: 10.1073/pnas.1909653116

[51]. Gibson DG, Young L, Chuang R-Y, Venter JC, Hutchison CA 3rd, and Smith HO (2009) Enzymatic assembly of DNA molecules up to several hundred kilobases. Nat. Methods 6, 343–345. DOI: 10.1038/nmeth.1318 [PubMed: 19363495]

[52]. Norville JE, Kelly DF, Knight TF, Belcher AM, and Walz T (2011) Fast and easy protocol for the purification of recombinant S-layer protein for synthetic biology applications. Biotechnol. J 6, 807–811. DOI: 10.1002/biot.201100024 [PubMed: 21681963]

[53]. Tian B, Fernandez-Bravo A, Najafiaghdam H, Torquato NA, Altoe MVP, Teitelboim A, Tajon CA, Tian Y, Borys NJ, Barnard ES, Anwar M, Chan EM, Schuck PJ, and Cohen BE (2018) Low irradiance multiphoton imaging with alloyed lanthanide nanocrystals. Nat. Commun 9, 3082. DOI: 10.1038/s41467-018-05577-8 [PubMed: 30082844]

[54]. Ostrowski AD, Chan EM, Gargas DJ, Katz EM, Han G, Schuck PJ, Milliron DJ, and Cohen BE (2012) Controlled synthesis and single-particle imaging of bright, sub-10 nm lanthanide-doped upconverting nanocrystals. ACS Nano 6, 2686–2692. DOI: 10.1021/nn3000737 [PubMed: 22339653]

[55]. Tajon CA, Yang H, Tian B, Tian Y, Ercius P, Schuck PJ, Chan EM, and Cohen BE (2018) Photostable and efficient upconverting nanocrystal-based chemical sensors. Opt. Mater 84, 345–353. DOI: /10.1016/j.optmat.2018.07.031

[56]. Mann VR, Powers AS, Tilley DC, Sack JT, and Cohen BE (2018) Azide–Alkyne Click Conjugation on Quantum Dots by Selective Copper Coordination. ACS Nano 12, 4469–4477. DOI: 10.1021/acsnano.8b00575 [PubMed: 29608274]

[57]. Schindelin J, Arganda-Carreras I, Frise E, Kaynig V, Longair M, Pietzsch T, Preibisch S, Rueden C, Saalfeld S, Schmid B, Tinevez J-Y, White DJ, Hartenstein V, Eliceiri K, Tomancak P, and Cardona A (2012) Fiji: an open-source platform for biological-image analysis. Nat. Methods 9, 676–682. DOI: 10.1038/nmeth.2019 [PubMed: 22743772]

[58]. Love JC, Estroff LA, Kriebel JK, Nuzzo RG, and Whitesides GM (2005) Self-assembled monolayers of thiolates on metals as a form of nanotechnology. Chem. Rev 105, 1103–1169. DOI: 10.1021/cr0300789 [PubMed: 15826011]

[59]. Howorka S, Sára M, Wang Y, Kuen B, Sleytr UB, Lubitz W, and Bayley H (2000) Surface-accessible residues in the monomeric and assembled forms of a bacterial surface layer protein. J. Biol. Chem 275, 37876–37886. DOI: 10.1074/jbc.M003838200 [PubMed: 10969072]

[60]. Han G, Mokari T, Ajo-Franklin C, and Cohen BE (2008) Caged quantum dots. J Am Chem Soc 130, 15811–15813. DOI: 10.1021/ja804948s [PubMed: 18983148]

[61]. Pellegrino T, Manna L, Kudera S, Liedl T, Koktysh D, Rogach AL, Keller S, Rädler J, Natile G, and Parak WJ (2004) Hydrophobic Nanocrystals Coated with an Amphiphilic Polymer Shell: A General Route to Water Soluble Nanocrystals. Nano Lett. 4, 703–707. DOI: 10.1021/nl035172j

[62]. Aroca RF (2013) Plasmon enhanced spectroscopy. Phys. Chem. Chem. Phys 15, 5355–5363. DOI: 10.1039/c3cp44103b [PubMed: 23493861]

[63]. He H, Xie C, and Ren J (2008) Nonbleaching fluorescence of gold nanoparticles and its applications in cancer cell imaging. Anal. Chem 80, 5951–5957. DOI: 10.1021/ac8005796 [PubMed: 18590338]

[64]. Cherns D (2017) High-Resolution Transimission Electron Microscopy of Surfances and Interfaces, in Analytical Techniques for Thin Films: Treatise on Materials Science and Technology (Tu KN, and Rosenberg R, Eds.), pp. 297–336, Academic Press. San Diego.

[65]. Luo D, Yan C, and Wang T (2015) Interparticle Forces Underlying Nanoparticle Self-Assemblies. Small 11, 5984–6008. DOI: 10.1002/smll.201501783 [PubMed: 26436692]

[66]. Gonzalez Garcia A, Nagelkerke MMB, Tuinier R, and Vis M (2020) Polymer-mediated colloidal stability: on the transition between adsorption and depletion. Adv Colloid Interface Sci 275, 102077. DOI: 10.1016/j.cis.2019.102077 [PubMed: 31816521]

[67]. Wu S, Han G, Milliron DJ, Aloni S, Altoe V, Talapin DV, Cohen BE, and Schuck PJ (2009) Non-blinking and photostable upconverted luminescence from single lanthanide-doped nanocrystals. Proc. Natl. Acad. Sci. U. S. A 106, 10917–10921. DOI: 10.1073/pnas.0904792106 [PubMed: 19541601]

[68]. Thal LB, Mann VR, Sprinzen D, McBride JR, Reid KR, Tomlinson ID, McMahon DG, Cohen BE, and Rosenthal SJ (2020) Ligand-conjugated quantum dots for fast sub-diffraction protein tracking in acute brain slices. Biomaterials Science 8, 837–845. DOI: 10.1039/C9BM01629E [PubMed: 31790090]

[69]. Sugiyama N, Sonay AY, Tussiwand R, Cohen BE, and Pantazis P (2018) Effective Labeling of Primary Somatic Stem Cells with BaTiO3 Nanocrystals for Second Harmonic Generation Imaging. Small 14, 1703386. DOI: 10.1002/smll.201703386

[70]. Lee C, Xu EZ, Liu Y, Teitelboim A, Yao K, Fernandez-Bravo A, Kotulska AM, Nam SH, Suh YD, Bednarkiewicz A, Cohen BE, Chan EM, and Schuck PJ (2021) Giant nonlinear optical responses from photon-avalanching nanoparticles. Nature 589, 230–235. DOI: 10.1038/s41586-020-03092-9 [PubMed: 33442042]

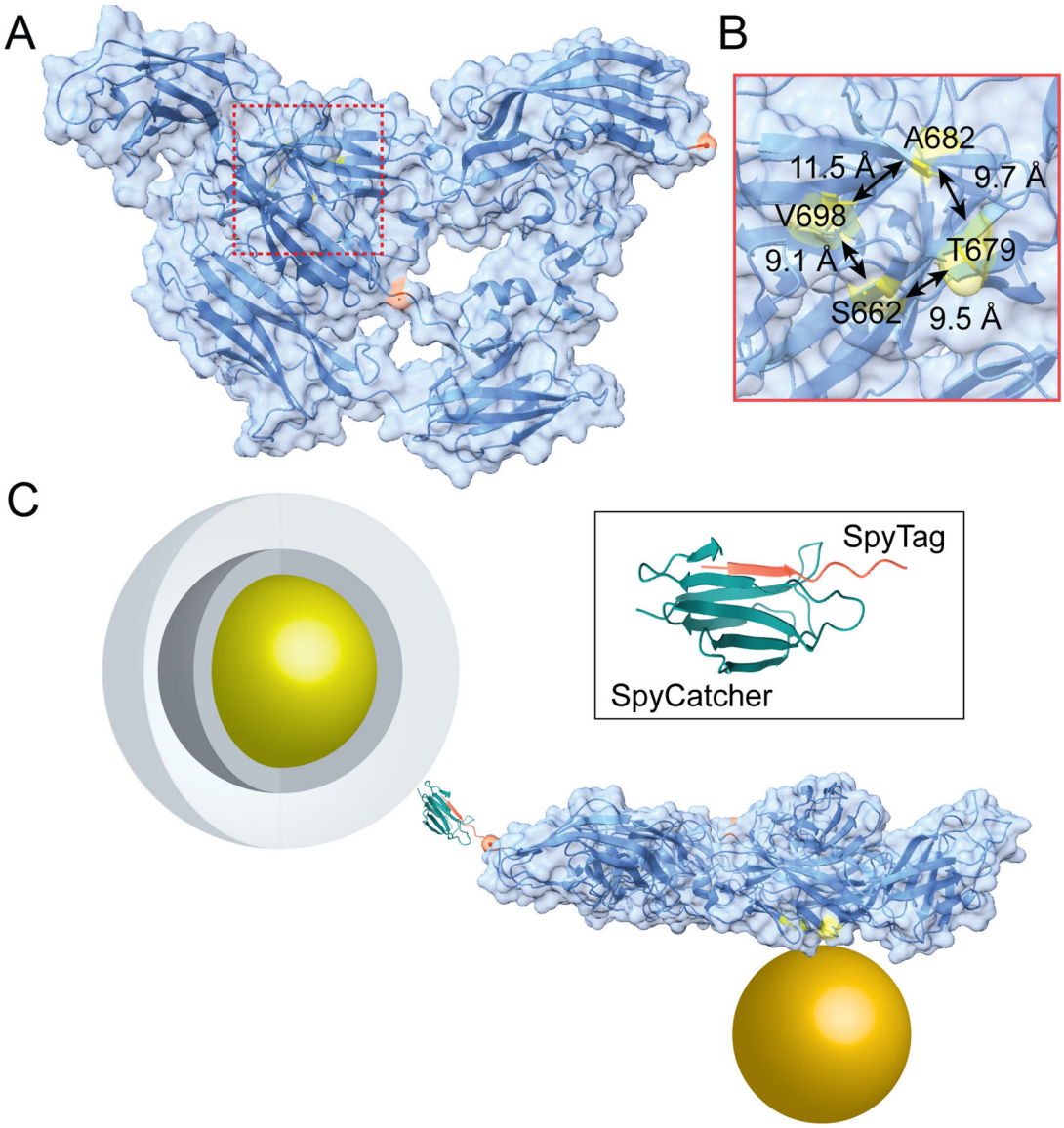

Figure 1.

Modified SbsB 2D assemblies conjugate diverse nanoparticles.

A) Structure of SbsB monomer (adapted from ref. 35) with NP attachment sites highlighted. Spy- or Snoop-Catcher peptide insertion sites (highlighted orange) after middle pore loop Val386, and after C-terminal Ser922. B) Tetra-Cys cluster (red box on reverse face in A) residues highlighted in yellow with inter-residue distances. C) Simultaneous quantum dot and 5-nm AuNP conjugation to SbsB monomer. QD is core/shell CdSe/ZnS (yellow and dark gray) passivated with amphiphilic polymer (light gray) conjugated to SpyCatcher (teal). SpyCatcher is conjugated to C-terminal SpyTag (orange) at C-terminus of SbsB. (*Inset*) SpyCatcher-SpyTag conjugate structure, adapted from ref. 43.

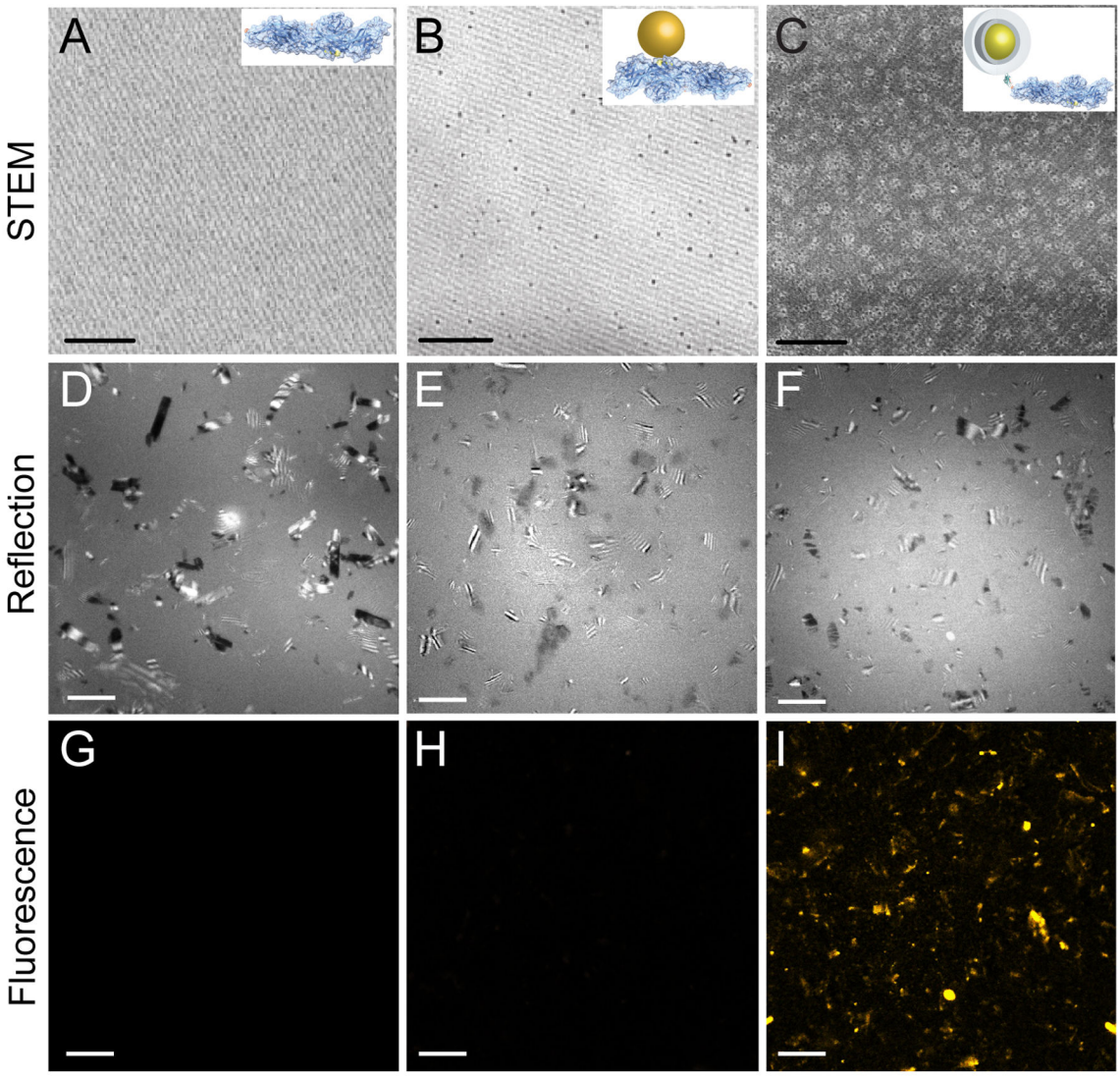

Figure 2.

Specificity of conjugation of AuNPs and quantum dots to SbsB nanosheets.

STEM images of SbsB-Cys4 nanosheets before (A) and after (B) conjugation to 5-nm AuNPs. C) STEM image of QD-SpyCatcher conjugated to SbsB-SpyTag nanosheets. Insets in (A-C) show schematics of respective couplings, and scale bars are each 100 nm. Interference reflection microscopy images (D-F) and confocal microscopy images (G-I) of SbsB sheets incubated with CdSe/ZnS QDs. (D) and (G) are SbsB-SpyTag nanosheets incubated with QDs without surface SpyCatcher. (E) and (H) are QD-Spycatcher incubated with SbsB nanosheets without SpyTags. (F) and (I) are SbsB-SpyTag nanosheets incubated with QD-Spycatcher conjugates. QDs with 585-nm emission peaks were imaged with 405 nm excitation. Scale bars in D-I are each 10 μm.

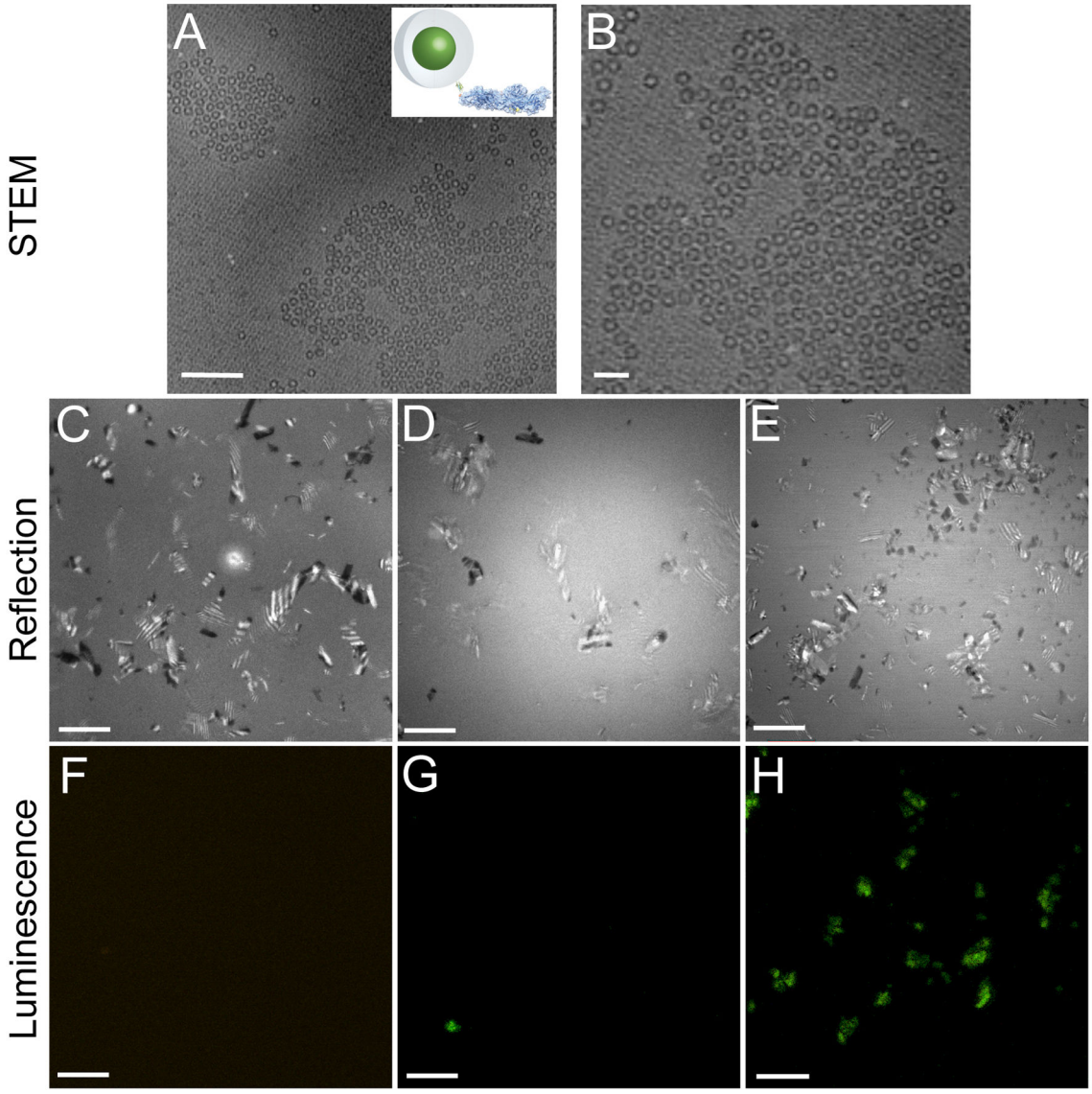

Figure 3.

Specific conjugation of UCNPs to SbsB nanosheets with SnoopTag/Catcher.

A) STEM image of SbsB-SnoopTag nanosheets coupled to SnoopCatcher-functionalized 16 nm $NaYF_4$ UCNPs doped with 20% Yb^{3+} and 2% Er^{3+}. Scale bar is 100 nm. B) Detail from (A). Scale bar is 50 nm. Interference reflection microscopy images (C-E) and upconverted UCNP luminescence (F-H). (C) and (F) are SbsB-SnoopTag nanosheets incubated with UCNPs without surface SnoopCatcher. (D) and (G) are UCNP-Snoopcatcher incubated with SbsB nanosheets without SnoopTags. (E) and (H) are SbsB-SnoopTag nanosheets incubated with UCNP-Snoopcatcher conjugates. UCNPs were excited at 980 nm. Scale bars in C-H are each 10 μm.

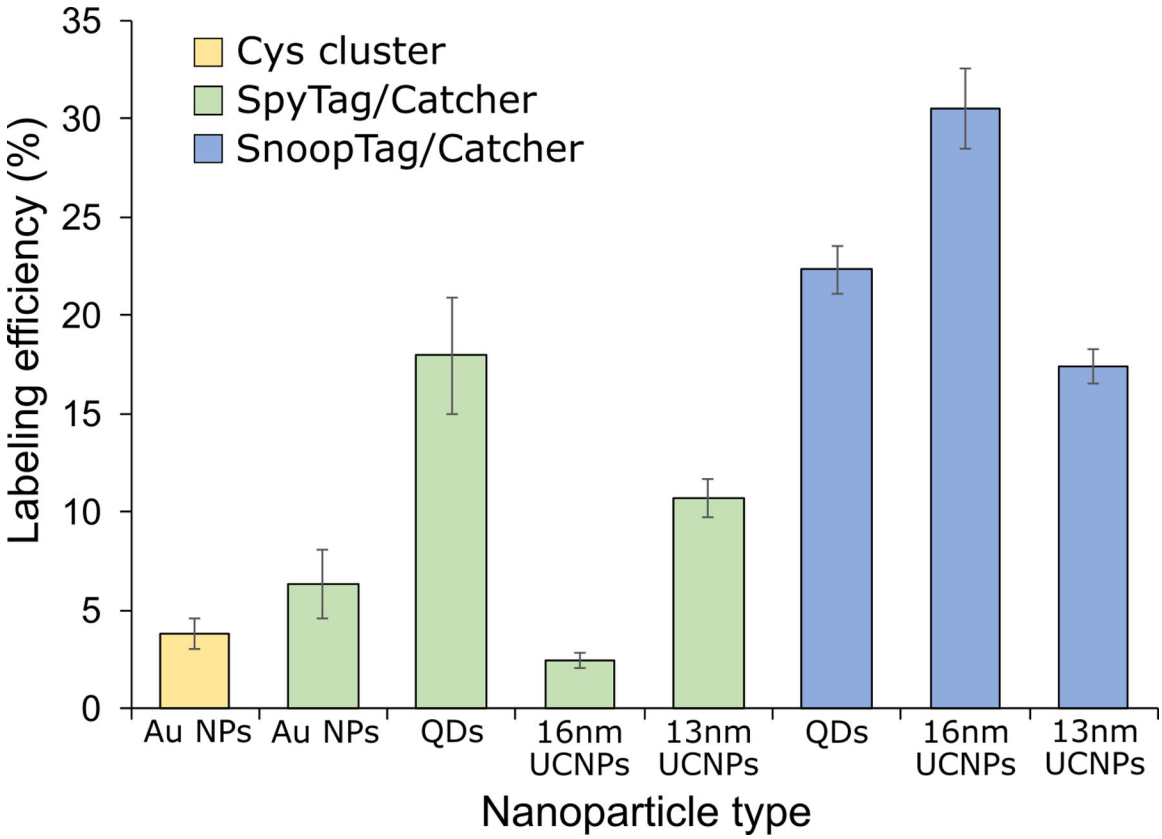

Figure 4.

Efficiencies of nanoparticle conjugation to SbsB nanosheet scaffolds.

Fraction of conjugation sites occupied by NPs, calculated from STEM images based on SbsB dimensions. Error bars are one standard deviation from the mean ($N = 9$ sheets for each NP conjugation).

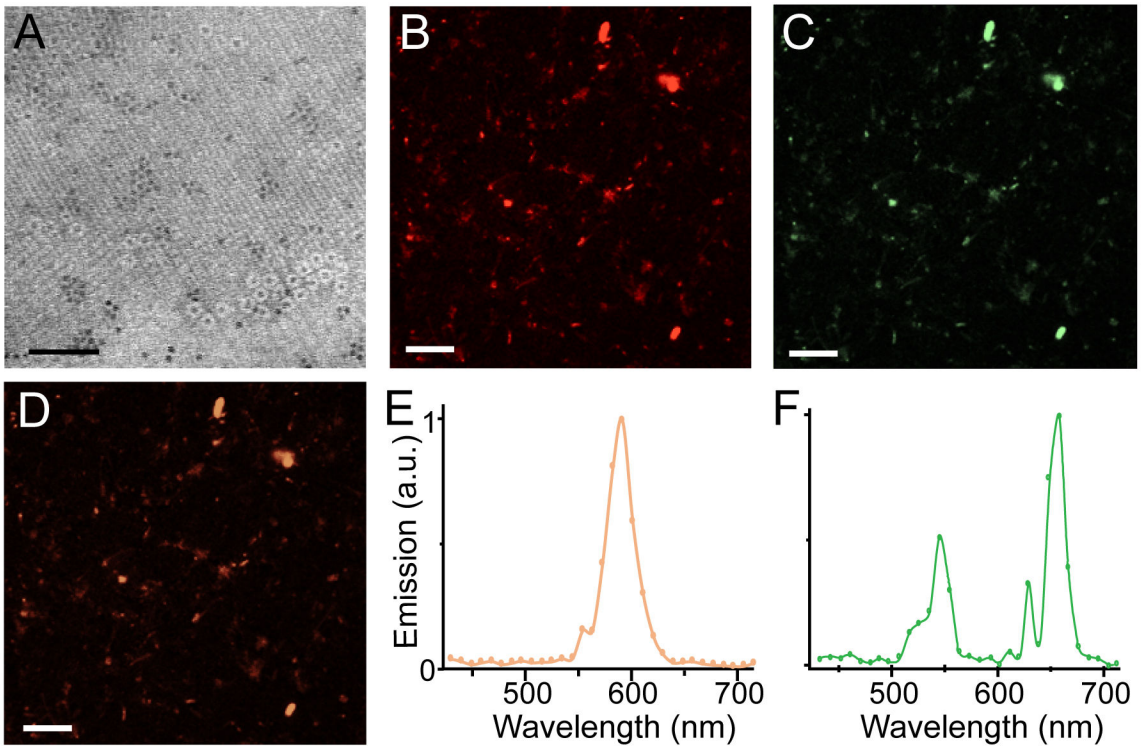

Figure 5.

Simultaneous conjugation of QDs and UCNPs to S-layer nanosheets.

A) STEM image of SpyTag- and SnoopTag-bearing SbsB sheets conjugated to both UCNP-SnoopCatcher and QD-SpyCatcher. SpyTag is inserted in the pore loop after Val386 and SnoopTag at the C-terminus after Ser922. Scale bar is 100 nm. B-D) Confocal imaging of UCNP- and QD-labeled SbsB sheets, excited at 405 nm for CdSe/ZnS QDs (B) or 980 nm for Yb^{3+}/Er^{3+} UCNPs (C). D) Merged image of (B) and (C). (E) Image spectrum of QD nanosheets in (B). (F) Image spectrum of UCNP nanosheets in (C). Scale bars in B-D are 10 μm.

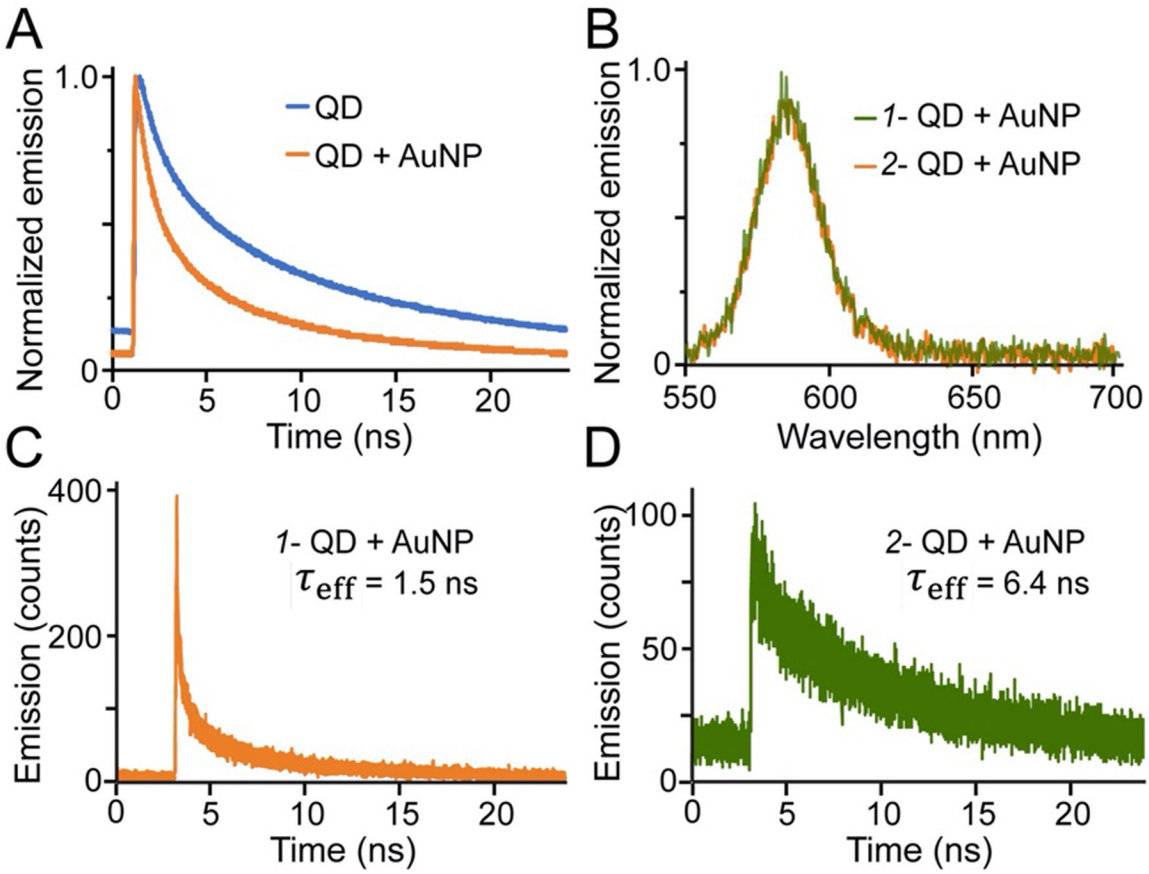

Figure 6.

Plasmonic interactions of colocalized QDs and AuNPs on S-layer nanosheets.

A) Fluorescence lifetime imaging of ensembles of SbsB nanosheets conjugated to QDs alone or to both QDs and AuNPs. Effective lifetimes τ_{eff} are 8.4 ns and 4.6 ns, respectively. (B) Image spectrum of 2 different regions of SbsB nanosheets conjugated to both QDs and AuNPs. (C) Radiative decay of QDs in region 1 of QD- and AuNP-conjugated nanosheets from (B), with biexponential lifetime components of 0.26 ns and 4.3 ns. (D) Radiative decay of QDs in region 2 from (B), with a single exponential fit of 6.4 ns.